



Contents lists available at ScienceDirect

European Journal of Mechanics B/Fluids

journal homepage: www.elsevier.com/locate/ejmflu

Merging of two helical vortices

Ivan Delbende^{a,b,*}, Benjamin Piton^{a,b}, Maurice Rossi^{a,c}^a Sorbonne Universités, UPMC Univ Paris 06, UFR919, F-75005 Paris, France^b LIMSI—CNRS, UPR 3251, BP 133, F-91403 Orsay Cedex, France^c CNRS, UMR 7190, d'Alembert—UPMC, F-75005 Paris, France

ARTICLE INFO

Article history:

Available online xxxx

Keywords:

Vortex

Helical vortex

Vortex merging

Vortex dynamics

ABSTRACT

Vortex merging is a basic fluid phenomenon which has been much studied for two-dimensional flows. Here we extend such a study to a specific class of three-dimensional flows, namely to vortices possessing a helical symmetry. In addition to the standard Reynolds number, this introduces another dimensionless control number, the pitch, which quantifies the periodicity length along the helix axis. Helical vortices with large pitches merge very much as in a two-dimensional setting. However, their rotation speed is reduced and the merging period is delayed. These effects, caused by the presence of a self-induced velocity in curved three-dimensional vortices, are understood by computing the streamfunction in the frame of reference rotating with the two vortices, and by inspecting the locations of its hyperbolic points. At intermediate pitch values, only viscous diffusion acts, resulting in a slow viscous type of merging. Finally for small pitches, the system is unstable resulting, at the nonlinear stage, in a different type of merging which breaks the initial central symmetry.

© 2014 Elsevier Masson SAS. All rights reserved.

1. Introduction

In the wake of propellers [1], wind turbines [2] or helicopters [3], a complex system of vortices is shed possessing the features of general three-dimensional flows: (1) multiple interacting vortices and (2) each vortex being characterized by curvature and torsion. These flows however are somewhat simpler: at least locally, they satisfy a helical symmetry, i.e. these vortices are invariant through combined axial translation and rotation. Many works have already been devoted to this specific class of flows. Steady rotating states' vortices have been described in analytical [4] and numerical [5] works, but they are mostly restricted to inviscid filaments and patches.

In this three-dimensional helical context [6], the process of vortex merging is of importance. For instance, it plays a role in the spatial evolution from the near- to the far-wake régime. Vortex merging has been much studied in two-dimensional flows where it is known to be the building-block of the inverse turbu-

lence cascade. Within the inviscid approximation, nonlinear equilibrium states of two vortices can be analyzed according to their size a and the distance d between their centroids. This provides a critical threshold for merging initiation, in terms of the ratio a/d . Introduction of viscosity however is necessary to follow the evolution in time between the different stages (quasi-equilibrium, merging itself) and to provide a description of the vortex observed once merging has been completed. We discuss here the merging of two identical three-dimensional vortices with the restriction of helical symmetry. Such a system is related to those observed behind a propeller or a turbine with 2 blades, and its merging dynamics is pertinent to understand vortex-grouping events observed in the far wake [1].

With respect to the two-dimensional case, a new feature is present in helical cases which changes the overall dynamics: each vortex is capable of rotating by itself. These helical 3D dynamics are simulated using a direct numerical simulation (DNS) code with built-in helical symmetry [7]. This code allows one to investigate the viscous dynamics of distributed vorticity profiles, the three-dimensional effects of vortex curvature and torsion being taken into account. The use of 2D-like numerical techniques makes it possible to reach higher Reynolds numbers and large evolution times when compared to a full 3D DNS.

* Corresponding author at: Sorbonne Universités, UPMC Univ Paris 06, UFR919, F-75005 Paris, France.

E-mail addresses: Ivan.Delbende@limsi.fr, Ivan.Delbende@upmc.fr (I. Delbende).

<http://dx.doi.org/10.1016/j.euromechflu.2014.04.005>

0997-7546/© 2014 Elsevier Masson SAS. All rights reserved.

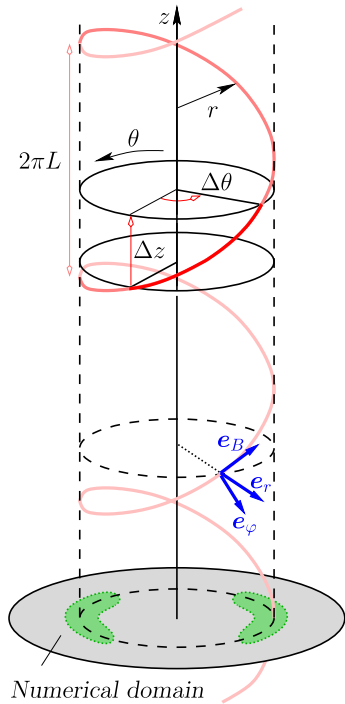


Fig. 1. Local helical basis.

2. Governing equations

2.1. Helical symmetry for incompressible flows

The vortices shed in the wake of a two-blade propeller are at least locally helically symmetric. As a simplifying hypothesis, we will assume the flow to strictly satisfy *helical symmetry of helix pitch* $2\pi L$ along a given axis. This means that the velocity field is invariant under the combination of an axial translation of Δz and a rotation of angle $\Delta\theta = \Delta z/L$ around the same axis (Fig. 1). The flow characteristics are hence identical along the helical lines $\theta - z/L = \text{const}$. Positive (resp. negative) L values correspond to right-handed (resp. left-handed) helices. A scalar field is helically symmetric if it depends on only two space variables r and $\varphi \equiv \theta - z/L$. Helical symmetry for a vector field \mathbf{u} can be expressed as follows:

$$\mathbf{u} = u_r(r, \varphi, t)\mathbf{e}_r(\theta) + u_\varphi(r, \varphi, t)\mathbf{e}_\varphi(r, \theta) + u_B(r, \varphi, t)\mathbf{e}_B(r, \theta) \tag{1}$$

where the orthonormal Beltrami basis (see Fig. 1) is defined as

$$\mathbf{e}_B(r, \theta) = \alpha(r) \left[\mathbf{e}_z + \frac{r}{L}\mathbf{e}_\theta(\theta) \right], \quad \mathbf{e}_r(\theta), \tag{2}$$

$$\mathbf{e}_\varphi(r, \theta) = \mathbf{e}_B \times \mathbf{e}_r$$

with $\alpha(r) \equiv (1 + r^2/L^2)^{-1/2}$ taking values ranging from 1 at the axis to 0 at infinite radius.

In the above framework, a general incompressible helical flow can be expressed as

$$\mathbf{u} = u_B(r, \varphi, t)\mathbf{e}_B + \alpha(r)\nabla\psi(r, \varphi, t) \times \mathbf{e}_B \tag{3}$$

where $\psi(r, \varphi, t)$ is a streamfunction providing the two components $u_r(r, \varphi, t)$ and $u_\varphi(r, \varphi, t)$. In addition, the vorticity field reads

$$\boldsymbol{\omega} = \omega_B(r, \varphi, t)\mathbf{e}_B + \alpha\nabla\left(\frac{u_B(r, \varphi, t)}{\alpha}\right) \times \mathbf{e}_B. \tag{4}$$

Hence the total flow field is given by two scalar fields, namely $\omega_B(r, \varphi, t)$ the vorticity component along the unit vector \mathbf{e}_B and

$u_B(r, \varphi, t)$ the velocity component along the same vector. Indeed the streamfunction ψ is slaved to both ω_B and u_B by equation

$$\omega_B - \frac{2\alpha^2}{L}u_B = -\mathbb{L}\psi \tag{5}$$

where the linear operator \mathbb{L} is a generalized Laplace operator:

$$\mathbb{L}(\cdot) = \frac{1}{r\alpha} \frac{\partial}{\partial r} \left(r\alpha^2 \frac{\partial}{\partial r}(\cdot) \right) + \frac{1}{r^2\alpha} \frac{\partial^2}{\partial \varphi^2}(\cdot).$$

Using expression (2) the helical component of velocity is written as $u_B(r, \varphi, t) = \alpha(u_z + ru_\theta/L)$. At large radial distances, the ratio $u_B(r, \varphi, t)/\alpha$ thus tends towards the constant $U_z^\infty + \Gamma/(2\pi L)$, with $U_z^\infty = u_z(r = \infty)$ and Γ the total circulation in the fluid domain. Instead of $u_B(r, \varphi, t)$, it is thus convenient to use the quantity

$$u_H \equiv \frac{u_B}{\alpha} - \left(U_z^\infty + \frac{\Gamma}{2\pi L} \right),$$

which tends towards 0 when $r \rightarrow \infty$. Up to a multiplicative factor, the variable u_H corresponds to a longitudinal velocity or jet profile in the vortex core.

2.2. Navier–Stokes equations with helical symmetry

The dynamical equations can be thus formulated within a generalization of the standard 2D ψ - ω method. The equations for u_B and ω_B read as

$$\begin{aligned} \partial_t u_B + NL_u &= VT_u \\ \partial_t \omega_B + NL_\omega &= VT_\omega \end{aligned} \tag{6}$$

where the nonlinear terms and the viscous terms are given by

$$\begin{aligned} NL_u &\equiv \mathbf{e}_B \cdot [\boldsymbol{\omega} \times \mathbf{u}], & VT_u &\equiv \nu \left[\mathbb{L} \left(\frac{u_B}{\alpha} \right) - \frac{2\alpha^2}{L} \omega_B \right], \\ NL_\omega &\equiv \mathbf{e}_B \cdot \nabla \times [\boldsymbol{\omega} \times \mathbf{u}], & & \\ VT_\omega &\equiv \nu \left[\mathbb{L} \left(\frac{\omega_B}{\alpha} \right) - \left(\frac{2\alpha^2}{L} \right)^2 \omega_B + \frac{2\alpha^2}{L} \mathbb{L} \left(\frac{u_B}{\alpha} \right) \right]. \end{aligned} \tag{7}$$

The variable $\varphi = \theta - z/L$ being 2π -periodic, the numerical code uses Fourier series along that direction, and second order finite differences in the radial direction. The time advance is performed using second order backward discretization of the temporal derivative. Nonlinear terms explicitly appear through second order Adams–Bashforth extrapolation whereas the viscous terms are treated implicitly. At the boundary at $r = R_{\text{ext}}$, potential-flow conditions are imposed, so that the simulation mimics the vortex dynamics in a radially infinite flow domain. More details can be found in [7,8].

2.3. Vortex characterization and initial conditions

During simulations, each vortex is characterized by several features (Fig. 2). First, one locates the point where the maximum helical vorticity ω_B is reached in the plane $z = 0$ (denoted hereafter by Π_0). This point is determined by its radial $r_{\text{max}}(t)$ and angular position $\theta_{\text{max}}(t)$. This leads to an angular velocity $\Omega(t) = d\theta_{\text{max}}/dt$. Second, the vortex is described by the vorticity ω_B and velocity u_H distributions. When visualizing the complete vortex system, these quantities are displayed in the Π_0 plane. However, when the characteristics of a single vortex are considered, such fields can be better analyzed in a plane perpendicular to the vortex centerline, so that geometrical deformation effects occurring in the Π_0 plane are eliminated (see Fig. 2). The plane Π_\perp is thus introduced, which contains the point $(r_{\text{max}}(t), \theta_{\text{max}}(t), z = 0)$ and is perpendicular to the vector $\mathbf{e}_B^{\text{max}} \equiv \mathbf{e}_B(r_{\text{max}}(t), \theta_{\text{max}}(t))$. Using the invariance of ω_B

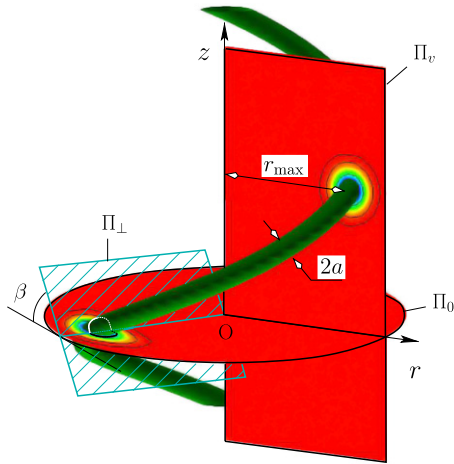


Fig. 2. Vortex geometry and characteristic planes.

and u_H along helical lines, it is possible to retrieve their values in the plane Π_{\perp} from those in the plane Π_0 . In analogy to the two-dimensional case, a core size $a(t)$ is then defined in the plane Π_{\perp} as a dispersion radius [9] of the quantity $\omega \cdot e_B^{\max}$.

By choosing adequate initial conditions, the problem can be made generic: one assumes that the flow at $t = 0$ results from the time evolution from $t = t_* < 0$ of two singular helical vortices of circulation Γ located at a radial distance R_* from the axis, and of helical reduced pitch L . Clearly the simulation cannot be initiated from this singular filament state. There exists a self-consistent procedure which is not detailed here that defines the adequate profile of each vortex: the condition at $t = 0$ consists of two identical vortices with an initial thin core a_0 , a pitch $2\pi L$, and a vorticity maximum located at θ_0 and $\theta_0 + \pi$ in the Π_0 plane. This procedure is based on a two-dimensional ansatz: the singular vortex filaments diffuse in their respective Π_{\perp} planes into 2D Gaussian profiles with core sizes $a_0 \approx \sqrt{-4\nu t_*}$. Based on this idea, we choose an initial ω_B distribution in the Π_0 plane such that the associated values of ω_B in the Π_{\perp} planes computed through the helicoidal symmetry indeed lead to such Gaussian profiles. The discussion about the initial u_H distribution is deferred to Section 3.4 (Eq. (12)).

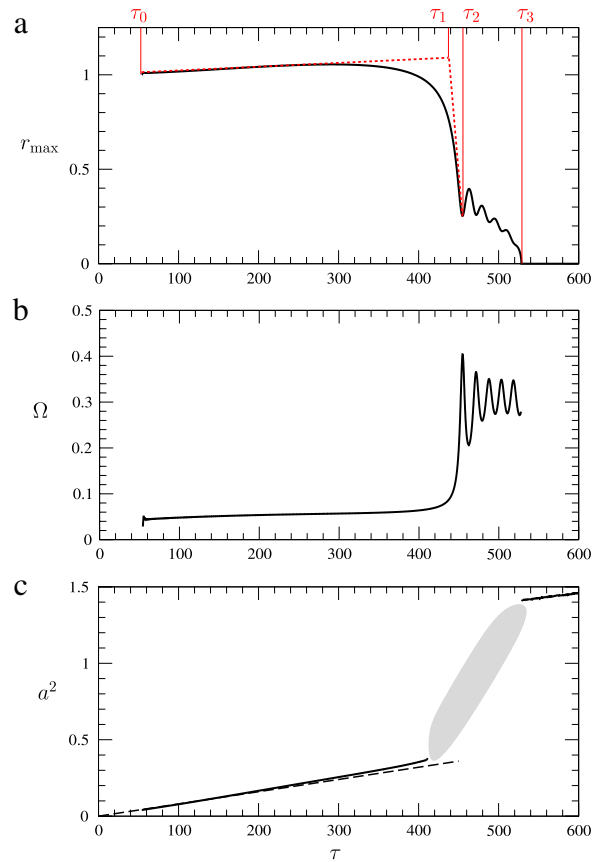


Fig. 4. Simulation for $L = 2.5$ and $Re = 5000$. (a) Radial position r_{\max} of the vorticity maximum as a function of time τ . The geometrical construction shown defines the time τ_1 , and times τ_2 and τ_3 are also displayed. (b) Angular velocity $\Omega(\tau)$. (c) Core size $a(\tau)$. During the phases where filamentation takes place, this quantity is not evaluated (shaded region).

In the following, in order to express the evolution from the singular state we always use the time $\tau = t - t_*$ and we adopt the quantities R_* and R_*^2/Γ as space and time scales. The dynamics is then governed by two dimensionless parameters: the Reynolds number $Re = \Gamma/\nu$ and the reduced pitch $\bar{L} \equiv L/R_*$. From now on,

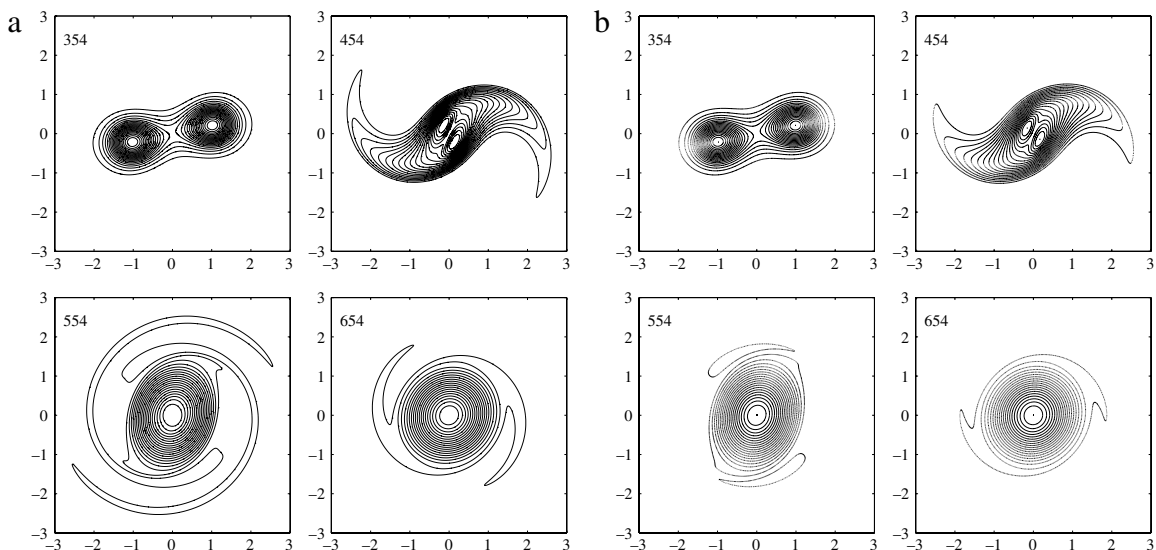


Fig. 3. Simulation for $L = 2.5$ and $Re = 5000$. Isocontours in the plane Π_0 of (a) $\alpha\omega_B$ (positive values) and (b) u_H (negative values) at dimensionless times $\tau = 354, 454, 554, 654$.

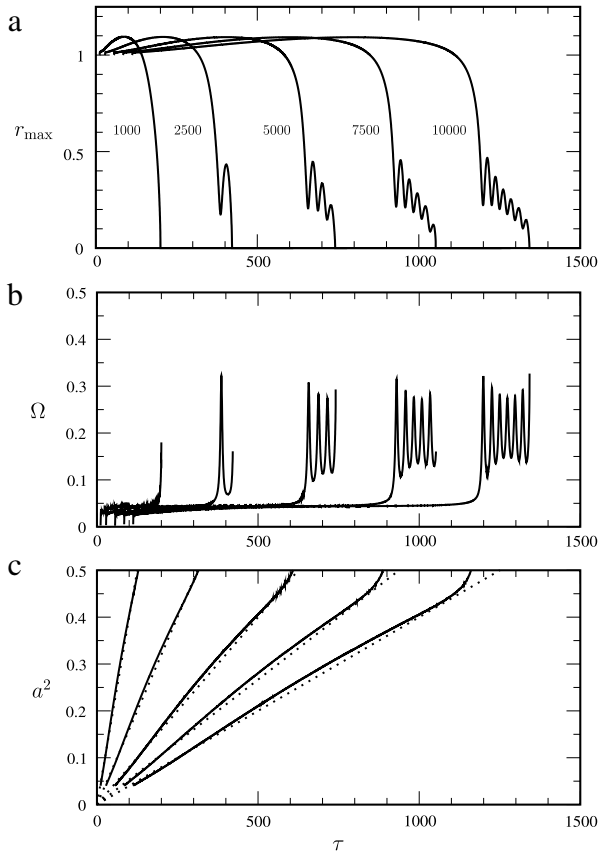


Fig. 5. Large pitch $L = 2$. Influence of the Reynolds number (Re values are indicated in the figures) on (a) the radial position r_{\max} of vorticity maximum versus time τ ; (b) the angular velocity $\Omega(\tau)$ of the vorticity maximum; (c) the square of the core size $a^2(\tau)$ (the dotted line corresponds to the 2D diffusion law $a^2(\tau) = 4\tau/\text{Re}$).

all quantities are dimensionless and we drop the bars above the corresponding variables for simplicity.

Simulations are performed in a numerical domain defined by a disk of dimensionless radius $R_{\text{ext}} = 3$. It was checked that no significant vorticity reaches the outer boundary, as potential-flow conditions are enforced there. However, for simulations at $L = 1.9$ and $L = 2$, it was found necessary to move the boundary to $R_{\text{ext}} = 4$. The domain is meshed by $N_r \times N_\theta$ grid points. For the Reynolds number $\text{Re} = 1000$, we choose $N_r = 256$ and $N_\theta = 192$; for $\text{Re} = 2500$, $N_r = 384$ and $N_\theta = 288$; for $\text{Re} = 5000$ and 10000 , $N_r = 512$ and $N_\theta = 384$.

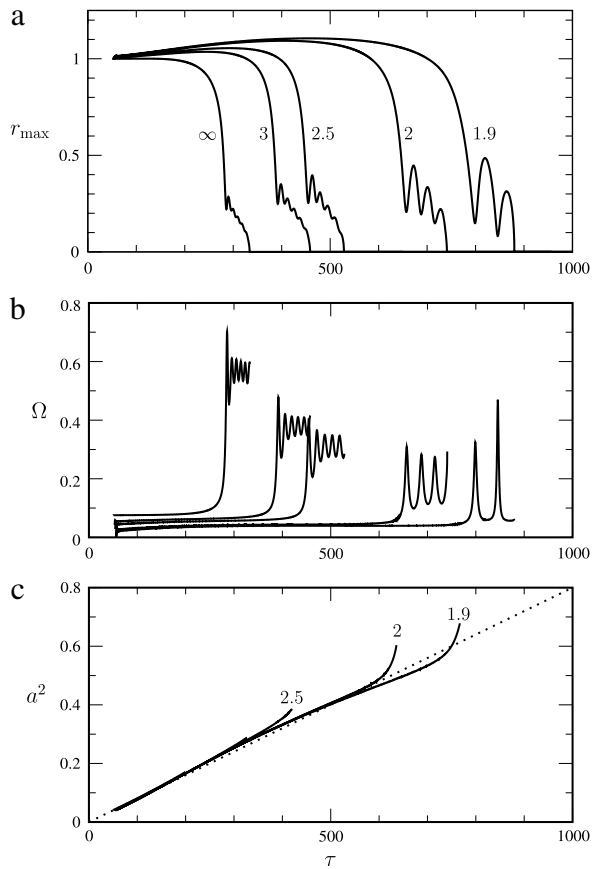


Fig. 7. Large pitch. Influence of L ($L = \infty, 3, 2.5, 2, 1.9$) for $\text{Re} = 5000$ on (a) the radial position r_{\max} of the vorticity maximum versus time τ ; (b) the angular velocity $\Omega(\tau)$ of the vorticity maximum; (c) the square of the core size $a^2(\tau)$ (the dotted line corresponds to the 2D diffusion law).

3. Merging of large pitch vortices $L \geq 1.9$

In this section, we consider two helical vortices with a large pitch, typically $L \geq 1.9$, and describe the merging process in that instance.

3.1. A typical case: $L = 2.5$, $\text{Re} = 5000$

The results plotted in Fig. 3 are typical for all $L \geq 1.9$ simulations. The vorticity $\alpha\omega_B$ and velocity u_H components are plotted in the plane Π_0 during a simulation at $L = 2.5$ and

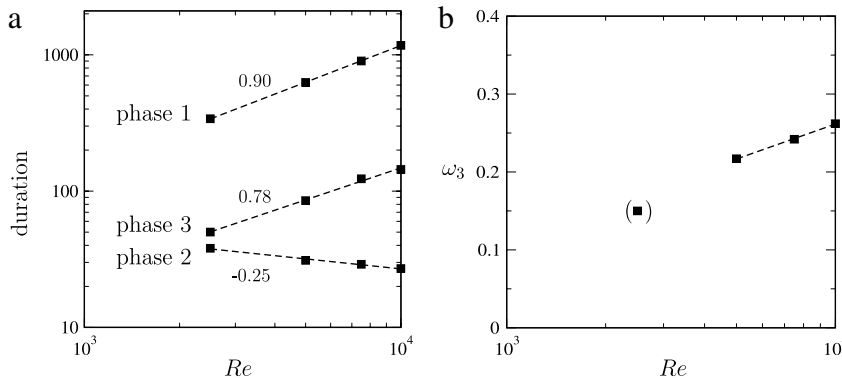


Fig. 6. Large pitch $L = 2$. (a) Influence of the Reynolds number Re on the duration of phases 1–3. A power law is obtained for each phase with an exponent written on the graph. (b) Oscillation frequency ω_3 during phase 3 as a function of Re . The bracketed value is based on only one oscillation. The dashed line corresponds to the scaling law $\omega_3 \sim C + \log \text{Re}^{0.064}$.

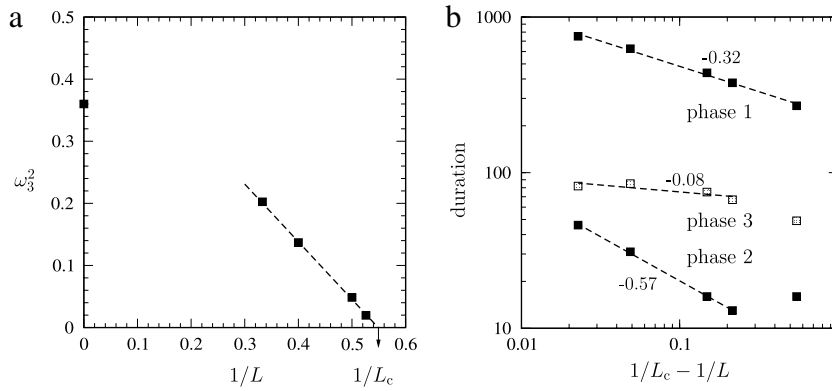


Fig. 8. Large pitch. (a) Square of the oscillation frequency ω_3 during phase 3 as a function of $1/L$. (b) Duration of phases 1–3 as a function of $L_c^{-1} - L^{-1}$. A power law is obtained with the exponent written on the graph.

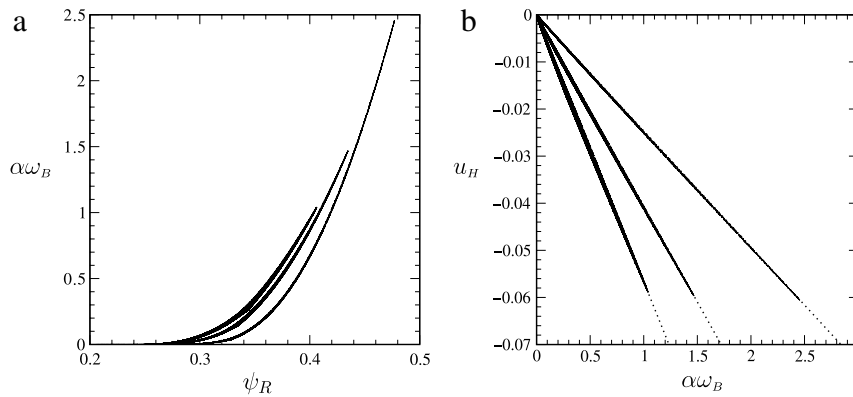


Fig. 9. Simulation for $L = 2.5$ and $Re = 5000$ for $\tau = 154, 254, 354$ (the curves move from right to left with increasing time τ). (a) Scatter plots for $\alpha\omega_B$ vs. ψ_R ; (b) scatter plots for u_H vs. $\alpha\omega_B$ (the dotted lines correspond to the analytical formula (11)).

$Re = 5000$. The initial central symmetry is preserved: vortices remain identical and given by a unique radial position $r_{max}(t)$ and two angular positions $\theta_{max}(t)$ and $\theta_{max}(t) + \pi$. Fig. 4 provides the value $r_{max}(t)$ as well as the angular velocity $\Omega(t)$ and core size $a(t)$. In a first phase (snapshot at $\tau = 354$ in Fig. 3(a) and (b)), vortices rotate counterclockwise and grow in size through viscous diffusion. During most of the phase, the two vortices slowly drift apart. A second phase of the dynamics follows in which the vortices move towards the center and their angular velocity drastically increases. As there is a continuous shift from phases 1 to 2, it is difficult to define a critical time τ_1 for the initiation of phase 2. Here we use the geometrical construction shown in Fig. 4(a) to define τ_1 (for the specific simulation $\tau_1 = 438$). This second phase ends at τ_2 where the value $r_{max}(t)$ reaches a first minimum (for the specific simulation, $\tau_2 = 454$). It is followed by a phase characterized by oscillations in which vortices are at a certain distance from the center (see snapshots at $\tau = 454$). Phase 2 ends at $\tau = \tau_3$ when $r_{max} = 0$ (for the specific simulation, $\tau_3 = 529$) leading to a single elliptical central vortex with the presence of filaments around the vortex core (snapshot at $\tau = 554$ in Fig. 3(a) and (b)). The fourth phase corresponds to the evolution towards the asymptotic diffusing Gaussian state (snapshots at $\tau = 654$ in Fig. 3(a) and (b)).

3.2. Influence of the Reynolds number

The influence of the Reynolds number on the dynamics is shown in Fig. 5 for $L = 2$. These effects remain valid for all cases with $L \geq 1.9$:

- Phase 1: the initial diffusion lasts longer as the Reynolds number is increased. It is observed from simulations that the

duration τ_1 is proportional to a power of Re at a fixed value of L (Fig. 6). For $L = \infty$, it evolves in Re , for $L = 2$ in $Re^{0.9}$. The angular velocity $\Omega(\tau)$ does not change with Re .

- Phase 2: distance $r_{max}(\tau_2)$ at the end of phase 2 weakly depends on the Reynolds number (see Fig. 5(a)). The duration $(\tau_2 - \tau_1)$ of this phase has a weak dependence on the Reynolds number: for instance at $L = 2$, $(\tau_2 - \tau_1) \sim Re^{-0.25}$.
- Phase 3: the frequency ω_3 of oscillations during phase 3 slightly increases with the Reynolds number. The duration $(\tau_3 - \tau_2)$ of this phase scales as a power of the Reynolds number. For $L = \infty$, it evolves in $Re^{0.5}$, for $L = 2$ in $Re^{0.78}$.

Finally, as seen in Fig. 5(c), the core size $a^2(\tau)$ evolves as a standard two-dimensional diffusion i.e. as $a^2(\tau) = 4\tau/Re$.

3.3. Influence of the helical pitch: angular velocity and merging

For large $L \geq 1.9$ values, decreasing the pitch L from $L = \infty$ has a marked slowdown effect on the merging process at a constant Reynolds number (Fig. 7). In particular, the vortices rotate at a weaker angular velocity (Fig. 7(b)). This reduced rotating speed for the vortex pair originates from the increasing role of the self-induced motion of each vortex. For a straight vortex ($L = \infty$), the self-induced velocity vanishes; in the presence of curvature (finite L), the self-induced velocity tends to make each vortex rotate clockwise [10]. This effect thus counterbalances the mutual interaction i.e. the one induced by the companion vortex, which is always present. The frequency ω_3 of oscillations during phase 3 tends to zero when L is decreased. It can be fitted as a function of $1/L$ (Fig. 8(a)): $\omega_3^2 \sim 0.93(L_c^{-1} - L^{-1})$ with $L_c = 1.82$. The pitch L_c provides a well-defined threshold value which separates

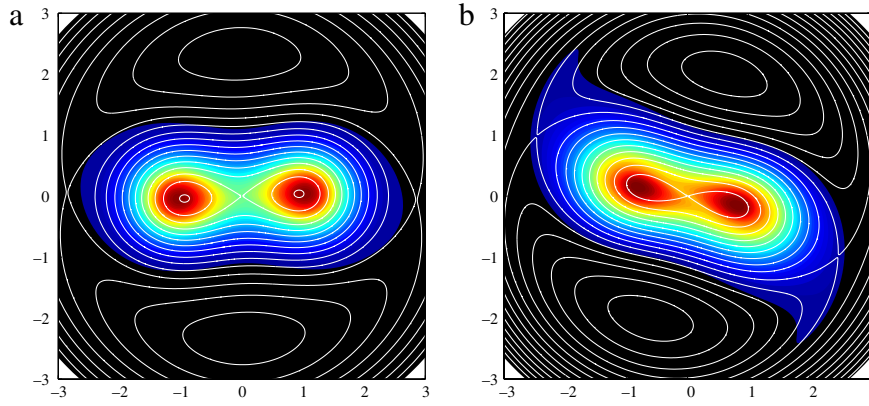


Fig. 10. Isocontours of vorticity component ω_B (colored and filled) and streamlines of ψ_R (white lines) for $L = 2$ at $Re = 5000$ (a) before critical time τ_1 and (b) just after critical time τ_1 .

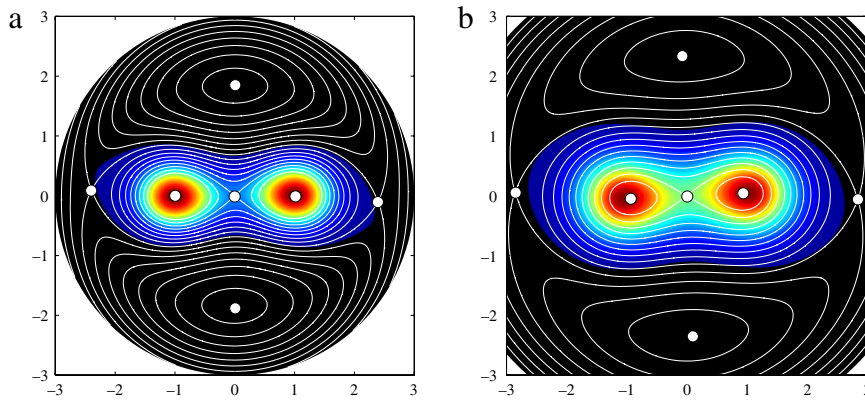


Fig. 11. Isocontours of vorticity component ω_B (colored and filled) and streamlines of ψ_R (white lines) for (a) $L = 3$ and (b) $L = 2$ at $Re = 5000$ near critical time τ_1 before the convective phase 2. The streamline pattern displays two types of hyperbolic points and two types of elliptic points. Note that the same scale is used for both graphs, although the sizes of the computational domain are (a) $R_{ext} = 3$ and (b) $R_{ext} = 4$.

the merging dynamics at large pitches from a different one at intermediate pitches. The durations of phases 1–3 all scale as powers of $(L_c^{-1} - L^{-1})$ (see Fig. 8(b)). By contrast, the core size is relatively unchanged by L (Fig. 7(c)).

3.4. Quasi-steady state before merging and merging onset

During phase 1, there exists a univoque dependency (see Fig. 9) between $\alpha\omega_B$ or u_H and ψ_R , the streamfunction defined in the frame of reference rotating with the vortices i.e.

$$\psi_R = \psi + \frac{r^2}{2}\Omega. \tag{8}$$

This feature is related to the presence of a quasi-equilibrium. For an inviscid dynamics, an equilibrium solution rotating with a constant angular velocity Ω exists. It has been shown [5] that, for this solution, the velocity $u_H(r, \varphi - \Omega t)$ is a univoque function of ψ_R :

$$u_H = F(\psi_R). \tag{9}$$

Most theoretical studies are based on this inviscid approximation with $u_H = 0$. In that even more specific case, $\alpha\omega_B$ is also a univoque function of ψ_R :

$$\alpha\omega_B = G(\psi_R). \tag{10}$$

Both conditions are satisfied here in a viscous context: during phase 1, the flow thus follows an inviscid quasi-equilibrium (see Fig. 9(a)). However, the vortex core size, angular velocity and

distribution evolve through viscous diffusion. It can be demonstrated¹ in a viscous context, that, if $u_H(\tau = 0) = 0$, then u_H evolves in time according to

$$u_H = -\frac{2\tau}{L Re} \alpha\omega_B. \tag{11}$$

This relation is also verified in the viscous simulation (see Fig. 9(b)). Note that, since $t = 0$ corresponds to $\tau = -t_*$, we use the following initial u_H distribution for the simulations:

$$u_H(r, \varphi, t = 0) = \frac{2 t_*}{L Re} \alpha\omega_B. \tag{12}$$

The maximum absolute value of u_H is thus initially small and remains so as time evolves: this weak jet component emerging through viscous effects is not thought to play any active dynamical role in the present context. Higher initial values of u_H corresponding to helical vortices with swirl are left for future studies.

In the two-dimensional case, phase 1 – and thus the merging onset – is associated with the existence of the above quasi-equilibrium state and/or its stability. Quantitatively, phase 1 persists until $a(\tau)/r_{max}(\tau)$ exceeds a threshold value [11]. For the helical case, the merging is delayed as $1/L$ is increased. Paradoxically, for a given time τ in phase 1, $r_{max}(\tau)$ slightly increases with increasing $1/L$ (Fig. 7(a)) and the vortex core size does not change

¹ A paper presenting the proof of relation (11) is about to be submitted.

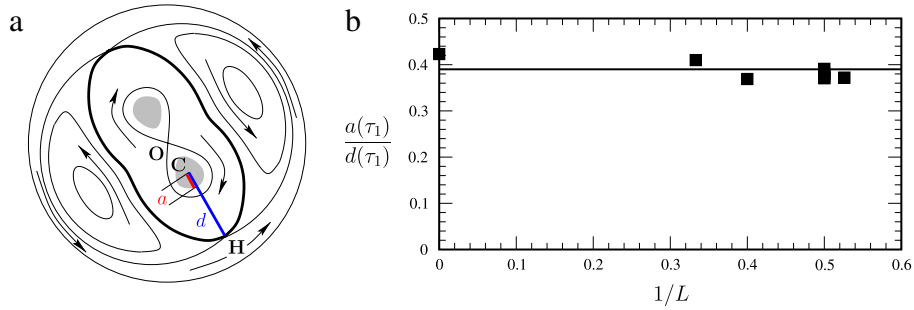


Fig. 12. (a) Definition of the distance d between vorticity maximum and the outer hyperbolic point of the co-rotating streamfunction ψ_R . (b) Critical value $a/d(\tau_1)$ as a function of $1/L$.

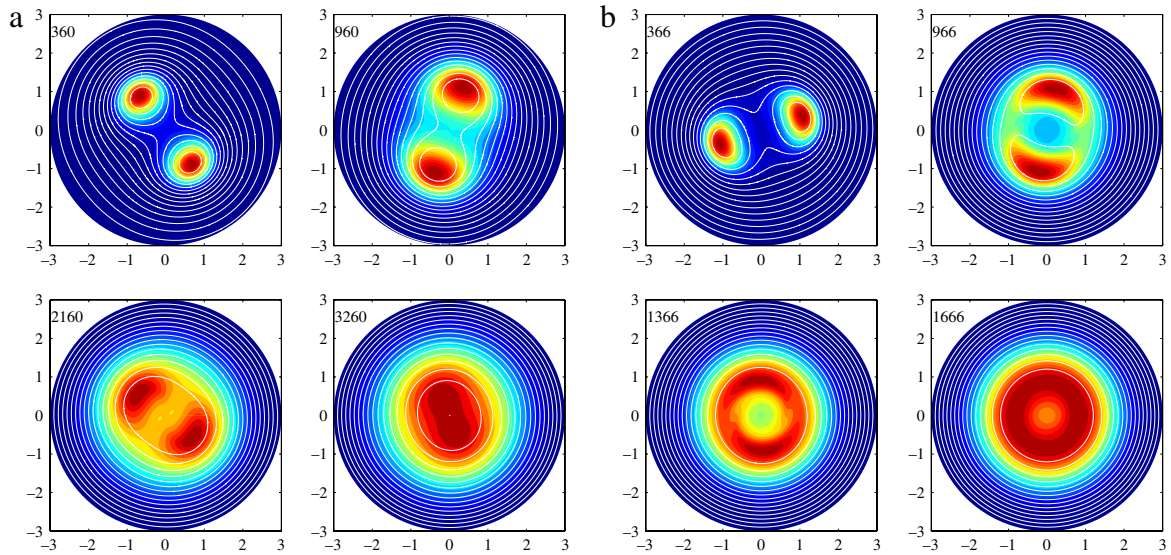


Fig. 13. Intermediate pitch and $Re = 5000$. Isocontours of vorticity component ω_B (colored and filled) and ψ_R (white lines). (a) $L = 1.5$ at times $\tau = 360, 960, 2160, 3260$. (b) $L = 1.2$ at times $\tau = 366, 966, 1366, 1666$.

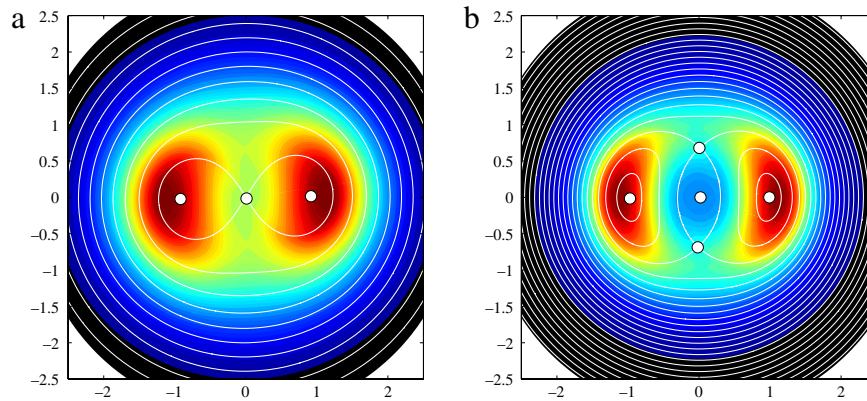


Fig. 14. Intermediate pitch and $Re = 5000$. Isocontours of ω_B (colored and filled) and ψ_R (white lines) and position of elliptic and hyperbolic points. (a) $L = 1.5$ at $\tau = 1561$. (b) $L = 1.2$ at $\tau = 866$.

with $1/L$ (see Fig. 7(c)) remaining close to the two-dimensional law $a^2(\tau) = 4\tau/Re$. Yet, the critical core size $a(\tau_1)$ at which phase 2 begins, increases as $1/L$ is increased. An explanation can be found by recalling the way the two-dimensional merging occurs for identical vortices: the convective merging phase 2 begins when a significant amount of vorticity has escaped the closed co-rotating streamlines of the two vortices, and begins to form filaments in the surrounding fluid [12–14]. A similar scenario takes place here, as shown in Fig. 10: at critical time τ_1 , vorticity has filled the atmosphere of the two vortices, and begins to escape into the peripheral

rotating fluid through the external hyperbolic points of the co-rotating streamfunction, because of viscous diffusion. The subsequent formation of filaments is believed to be associated with the convective phase 2 whereby vortices are radially pushed towards the axis. In Fig. 11, the hyperbolic points move towards larger r as soon as L is decreased. The critical core size thus increases together with d as L is decreased, which makes phase 1 last longer.

For different values of L and Re , the pertinent parameter for convective merging is not the ratio a/r_{max} , but rather the ratio between the core size a and the distance d between the vortex

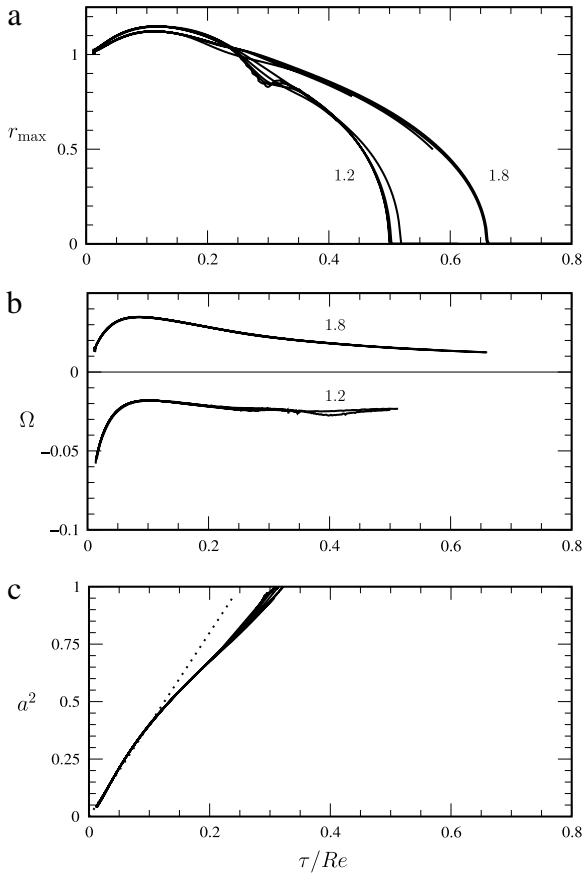


Fig. 15. Intermediate pitch $L = 1.8$ and $L = 1.2$. For a given L , the curves at various Reynolds numbers ($Re = 1000, 2500, 5000, 7500, 10\,000$) collapse when displayed in terms of τ/Re . (a) Radial position $r_{max}(\tau/Re)$ of the vorticity maximum; (b) angular velocity $\Omega(\tau/Re)$ of the vorticity maximum; (c) square of the core size $a^2(\tau/Re)$ (the dotted line represents the 2D diffusion law).

center and the outer hyperbolic point (see Fig. 12(a)). For the two-dimensional case, r_{max} and d are clearly related. As $1/L$ is increased, the rotation speed decreases thus causing the hyperbolic points of the co-rotating streamfunction to move away from the axis,

i.e. length d increases. It is observed from the simulations that, at critical time, the ratio $a/d(\tau_1)$ is almost constant and equals 0.39 (see Fig. 12(b)). This value is weakly dependent on the Reynolds number: for instance, at $1/L = 0.5$ in Fig. 12(b), the values $a/d(\tau_1)$ are plotted for several Reynolds numbers.

4. Diffusive merging at intermediate pitch $1.1 \leq L \leq 1.8$

As the helical pitch is decreased, the angular velocity computed in the DNS decreases and eventually becomes negative. The zone of intermediate pitch $1.1 \leq L \leq 1.8$ is thus characterized by weak vortex rotation, and the outer hyperbolic point is pushed away far from the axis, or does not exist at all. In that instance, neither filamentation nor convective merging can occur, and the behavior of the system is dominated by viscous diffusion which yields a slow, smooth merging process (Fig. 13). Actually, there exist two types of diffusive merging depending on whether L is larger or smaller than $L_d \approx 1.25$, corresponding to two different topologies of the streamlines in the co-rotating frame. For a first one $L \geq L_d$ (see the $L = 1.5$ case in Fig. 14(a)), the merging takes place at the axis, whereas for a second one $L \leq L_d$ (see the $L = 1.2$ case in Fig. 14(b)), the merging takes place at a radial distance of order unity and forms an axisymmetric corona of vorticity. In both cases, the flow keeps the initial central symmetry.

For the case $L \geq L_d$, a hyperbolic point for the streamlines is present at the center. On the contrary, for $L \leq L_d$, the center becomes elliptic and two hyperbolic points emerge away from the center, thus separating the central region and explaining why the vorticity concentrates along a corona. As a matter of fact, this latter merging occurs between coils rather than at the axis. For both cases, the flow is dominated by the diffusion effects, as shown by plotting the radial position r_{max} , angular velocity Ω and core size a^2 as functions of a rescaled time τ/Re (Fig. 15). Note however that the vortex core size now significantly departs from the two-dimensional viscous diffusion law.

5. Small pitch vortices $L \leq 1.1$: Okulov's instability

In the simulation at $L = 1$ displayed in Fig. 16(a), the system evolves similarly to the case of diffusive merging. However if this simulation is started with an initial perturbation (one vortex radially pushed by 0.001), the resulting evolution (see Fig. 16(b))

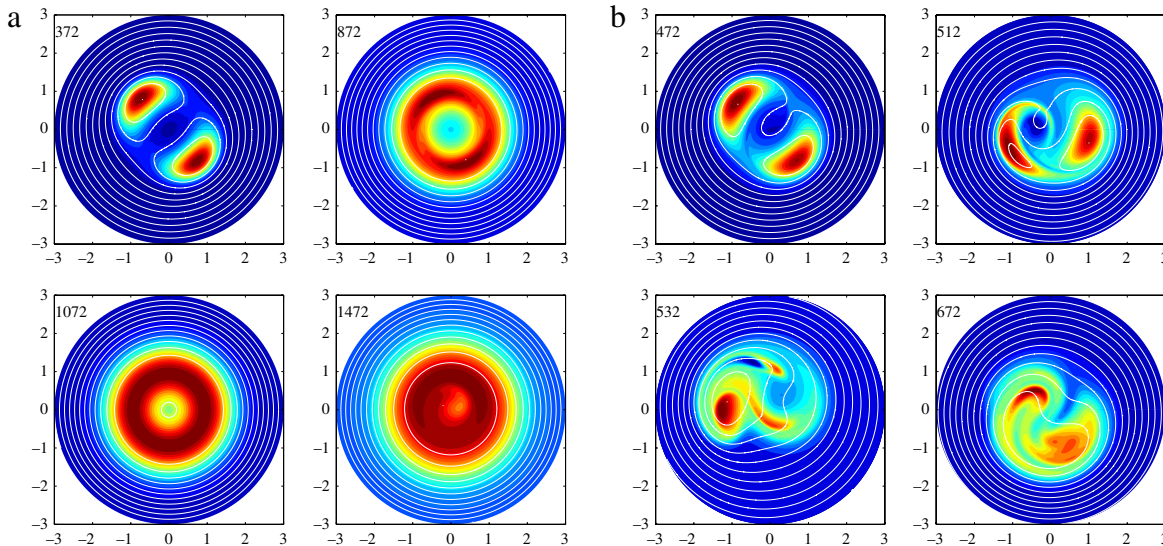


Fig. 16. Small pitch $L = 1$ and $Re = 5000$. (a) Isocontours of vorticity component ω_B (colored and filled) and ψ_B (white lines) at $\tau = 372, 872, 1072, 1472$. Here simulations are initiated without perturbation. (b) Isocontours of ω_B at $\tau = 472, 512, 532, 672$. Here, simulation starts from a state in which vortex positions have been moved by an amount 0.001.

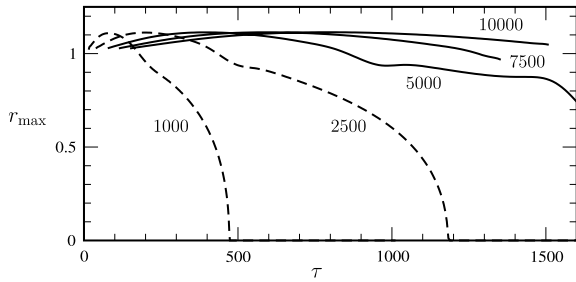


Fig. 17. Small pitch $L = 1$. Influence of the Reynolds number on the radial position r_{\max} of the vorticity maximum versus time τ . Here simulations are initiated without perturbation. Dashed lines correspond to an evolution into an axisymmetric state and continuous lines to an evolution dominated by symmetry-breaking instability. The case $Re = 5000$ is particular: it reaches an axisymmetric state but subsequent symmetry-breaking instability.

is quite different: an instability mechanism breaking the central symmetry between vortices is active, and its effects are clearly felt at $\tau = 472$. Indeed, at small pitches, a helical vortex pair is known to be unstable [15] for small core size filaments with respect to displacement modes, a phenomenon responsible for the destabilization of propeller and wind turbine wakes. The critical pitch under which such instability occurs for a vortex pair in the limit of small core sizes is $L_i = 1.106$. The present simulation indicates that this instability is not altered by finite core size.

Predicting precise frontiers between the diffusive and instability regimes is not an easy task since the instability growth rate depends on the vortex core size, which is a time-dependent quantity in viscous simulations. A closer inspection of the simulation started without initial perturbation (actually with a perturbation comparable to numerical precision) shows that the system forms a corona of vorticity through viscous diffusion before the

instability becomes observable (see $\tau = 1072$ in Fig. 16(a)). Hence for the lowest Reynolds numbers, the dynamics is essentially a diffusive merging process. Eventually however, it may happen that the instability becomes visible and slightly breaks the axisymmetry of the corona (snapshot at $\tau = 1472$). The influence of the Reynolds number is shown in Fig. 17.

In the simulations at lower pitches such as $L = 0.5$ (see Fig. 18), the growth rate of Okulov’s instability is more important and the system gets destabilized more rapidly: one helical vortex is strongly stretched (see at $\tau = 172$) and merges with the other ($\tau = 192$). It is remarkable that this behavior reminiscent of the vortex grouping observed in some experiments [1,16] can be described in the present helically symmetric framework. The present study essentially dealt with helical vortices initially located at $\theta = \theta_0$ and $\theta_0 + \phi$ with $\phi \approx \pi$. However, the numerical code is also able to tackle cases with ϕ quite different from π . Some runs were performed for such cases and led to merging dynamics similar to those presented in Fig. 18.

6. Conclusion

We numerically investigated the dynamics of a pair of identical helical viscous vortices with respect to their helical pitch and Reynolds number. At large pitch, vortex merging occurs that is analogous with the two-dimensional vortex merging: its underlying mechanism is due to the emission of vorticity filaments. In addition, a threshold for merging can be defined based on the external hyperbolic point position. At intermediate pitch $1.1 \leq L \leq 1.8$, the system rotates slowly around the axis, and diffusive effects dominate the dynamics. At smaller pitch $L \leq 1.1$, a slight shift of the initial vortex positions is able to rapidly destabilize the system leading to vortex grouping. The different types of merging in the (Re, L) plane are displayed in Fig. 19. Similar trends

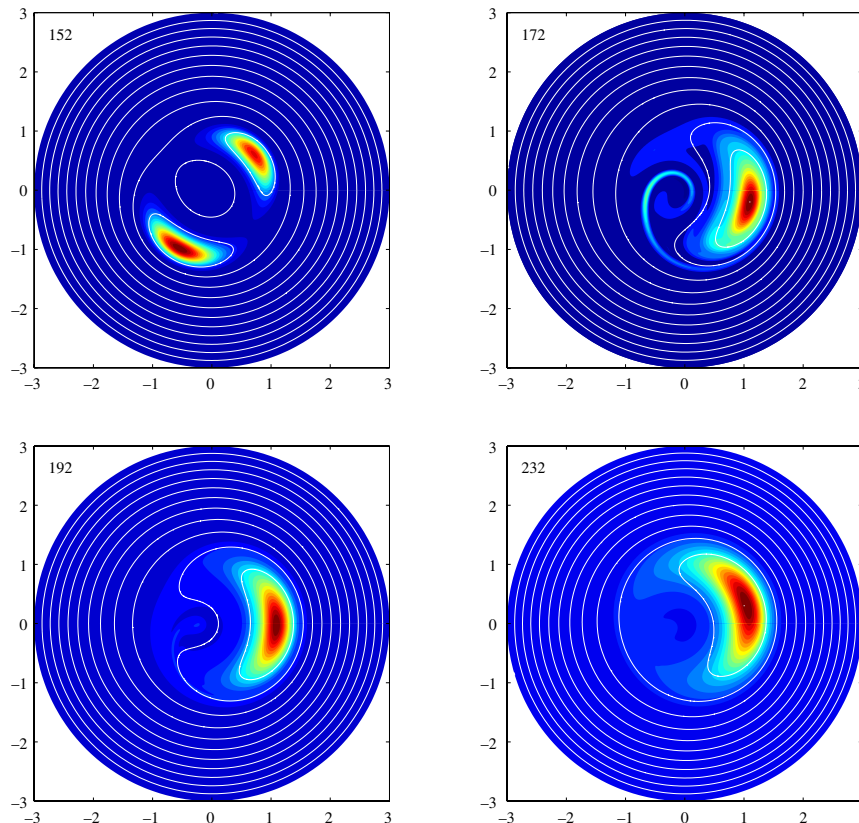


Fig. 18. Simulation for $L = 0.5$ and $Re = 5000$, starting from a state in which the vortex positions have been perturbed by an amount 0.001. Isocontours of vorticity component ω_B (colored and filled) and ψ_R (white lines) at $\tau = 152, 172, 192, 232$.

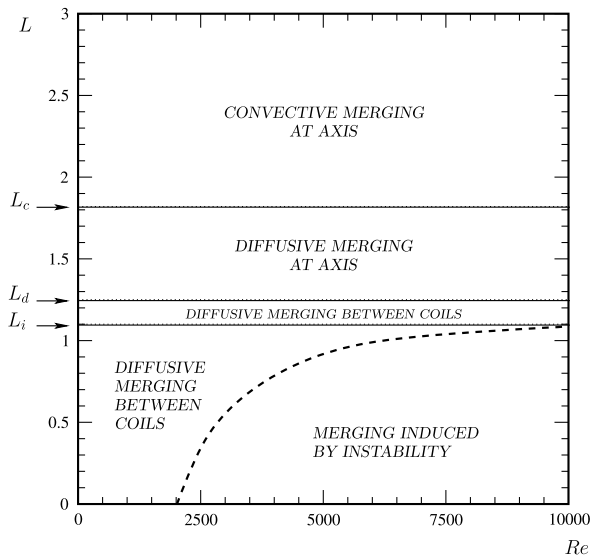


Fig. 19. Types of merging for two helical vortices, in the (Re, L) plane.

have been found for the three-helical vortex system [17]. In a future work, the influence of a hub vortex or of initial velocity u_H both present in practical simulations and experiments will be investigated and their role in the helical vortex dynamics will be determined. Furthermore, quasi-equilibrium rotating states obtained and described herein will define precise basic states to be used in a general linear stability analysis. In that framework, initial three-dimensional perturbations breaking the helical symmetry will be considered: this work will be hence performed in the spirit of Refs. [18,19], but in a viscous linear or nonlinear context.

Acknowledgments

This article is dedicated to our friend and colleague Patrick Huerre with whom two of us have been collaborating for quite a while. He was our cicerone along steep paths in the green valley of open flow instabilities. Thank you so much for that, dear Patrick!

This work was carried out with the financial support of the ANR (Agence Nationale de la Recherche) in the framework of

the project HELIX BLAN ANR-12-BS09-0023, using HPC resources from GENCI–IDRIS (grant 2013-2a1386), as well as computational facilities at LIMS–CNRS. Technical help from Jalel Chergui & Olivier Lassalle at LIMS is acknowledged.

References

- [1] M. Felli, R. Camussi, F. di Felice, Mechanisms of evolution of the propeller wake in the transition and far fields, *J. Fluid Mech.* 682 (2011) 5–53.
- [2] M.O.L. Hansen, J.N. Sørensen, S. Voutsinas, N. Sørensen, H.A. Madsen, State of the art in wind turbine aerodynamics and aeroelasticity, *Prog. Aerosp. Sci.* 42 (2006) 285–330.
- [3] B.G. Green, E.A. Gillies, R.E. Brown, The flow field around a rotor in axial descent, *J. Fluid Mech.* 534 (2005) 237–261.
- [4] P.A. Kuibin, V.L. Okulov, Self-induced motion and asymptotic expansion of the velocity field in the vicinity of a helical vortex filament, *Phys. Fluids* 10 (1998) 607–614.
- [5] D. Lucas, D.G. Dritschel, A family of helically symmetric vortex equilibria, *J. Fluid Mech.* 634 (2009) 245–268.
- [6] W.J. Devenport, C.M. Vogel, J.S. Zoldos, Flow structure produced by the interaction and merger of a pair of co-rotating wing-tip vortices, *J. Fluid Mech.* 394 (1999) 357–377.
- [7] I. Delbende, M. Rossi, O. Daube, DNS of flows with helical symmetry, *Theor. Comput. Fluid Dyn.* 26 (1) (2012) 141–160.
- [8] B. Piton, Simulations de tourbillons à symétrie hélicoïdale, Ph.D. Thesis, Sorbonne Universités, UPMC Univ Paris 06, 2011.
- [9] P.G. Saffman, *Vortex Dynamics*, Cambridge University Press, Cambridge, 1992.
- [10] S.V. Alekseenko, P.A. Kuibin, V.L. Okulov, *Theory of Concentrated Vortices: An Introduction*, Springer-Verlag, Berlin, 2007.
- [11] P. Meunier, U. Ehrenstein, T. Leweke, M. Rossi, A merging criterion for two-dimensional co-rotating vortices, *Phys. Fluids* 14 (8) (2002) 2757–2766.
- [12] M.V. Melander, N.J. Zabusky, J.C. McWilliams, Symmetric vortex merger in two dimensions: causes and conditions, *J. Fluid Mech.* 195 (1988) 305–340.
- [13] P. Meunier, S. Le Dizès, T. Leweke, Physics of vortex merging, *C. R. Phys.* 6 (2005) 431–450.
- [14] C. Cerretelli, C.H.K. Williamson, The physical mechanism for vortex merging, *J. Fluid Mech.* 475 (2003) 41–77.
- [15] V.L. Okulov, J.N. Sørensen, Stability of helical tip vortices in a rotor far wake, *J. Fluid Mech.* 576 (2007) 1–25.
- [16] T. Leweke, H. Bolnot, S. Le Dizès, Local and global pairing in helical vortex systems, in: *Proceedings of the International Conference on Aerodynamics of Offshore Wind Energy Systems and Wakes, ICOWES, Lyngby, Denmark, 2013*, pp. 94–101.
- [17] I. Delbende, M. Rossi, Dynamics of the three helical vortex system and instability, in: *Proceedings of the International Conference on Aerodynamics of Offshore Wind Energy Systems and Wakes, ICOWES, Lyngby, Denmark, 2013*, pp. 224–235.
- [18] S.E. Widnall, The stability of a helical vortex filament, *J. Fluid Mech.* 54 (1972) 641–663.
- [19] B.P. Gupta, R.G. Loewy, Theoretical analysis of the aerodynamic stability of multiple, interdigitated helical vortices, *AIAA J.* 12 (10) (1974) 1381–1387.